Earth and Planetary Science Letters 483 (2018) 64–75

Contents lists available at ScienceDirect

Earth and Planetary Science Letters

www.elsevier.com/locate/epsl

Time-dependent postseismic slip following the 1978 M_w 7.3 Tabas-e-Golshan, Iran earthquake revealed by over 20 years of ESA InSAR observations

Yu Zhou [a,b,*], Marion Y. Thomas [b], Barry Parsons [b], Richard T. Walker [b]

[a] Guangdong Provincial Key Laboratory of Geodynamics and Geohazards, School of Earth Sciences and Engineering, Sun Yat-sen University, Guangzhou 510275, China

[b] COMET, Department of Earth Sciences, University of Oxford, Oxford OX1 3AN, UK

ARTICLE INFO

Article history:
Received 2 October 2017
Received in revised form 26 November 2017
Accepted 1 December 2017
Available online 13 December 2017
Editor: R. Bendick

Keywords:
InSAR
Sentinel-1
time-dependent postseismic slip
1978 Tabas-e-Golshan earthquake
rate-and-state friction

ABSTRACT

We use over 20 yrs (1996–2017) of the European Space Agency's (ESA) radar interferometry (InSAR) observations to investigate the postseismic deformation of the Tabas fold segment following the 1978 M_w 7.3 Tabas-e-Golshan earthquake in eastern Iran. We generated maps of satellite line-of-sight (LOS) velocity using two ERS descending tracks (1996–1999), one Envisat descending track (2003–2010), one Sentinel-1A descending track (2014–2017) and one Sentinel-1A ascending track (2014–2017). The LOS velocity shows afterslip continuing for at least 40 yrs after the earthquake. Elastic dislocation modelling based on the InSAR measurements reveals a decrease in postseismic velocities from 5.0 ± 0.8 mm/yr in 1996–1999 to 3.9 ± 0.6 mm/yr in 2003–2005, 3.0 ± 0.4 mm/yr in 2006–2010, and a present rate of 2.3 ± 0.6 mm/yr in 2014–2017. The rates decay with time, t, as $1/t$, consistent with the predictions of a simple block-slider model. We then combine the InSAR rates and our previous estimates of the total earthquake slip derived from optical image matching and DEM differencing to explore the frictional behaviour of the Tabas fold. We obtained a rate-and-state parameter $a-b \approx 0.003$, indicating rate-strengthening frictional behaviour of the Tabas fault. We also inferred a minimum coseismic slip of 4.7 m, which might have driven bedding-plane shear at shallow depth, resulting in distributed fold growth and secondary faulting observed in the field. The results imply that both coseismic slip and afterslip have occurred in the same location. One possible mechanism to explain such a phenomenon is that the frictional parameter $a-b$ is small enough to allow dynamic ruptures to propagate into rate-strengthening regions.

1. Introduction

Recent advances in geodetic and seismic techniques have enabled us to document the broad variability in slip behaviour on active faults on which large earthquakes have occurred (e.g., Avouac, 2015; Segall et al., 2000; Şengör et al., 2005; Shen et al., 2009; Thomas et al., 2014a). Within the seismogenic depth, fault slip may be predominantly seismic in some places, i.e., displacement occurs during earthquakes (slip rate of m/s), or mainly aseismic in others as a result of steady (mm/yr to cm/yr) or transient creep (μm/s, i.e. 3×10^4 mm/yr, to mm/yr). In order to fully understand active faulting, it is therefore of prime importance to measure deformation accurately throughout the entire earthquake cycle.

Laboratory experiments suggest that, depending on the rock type, effective normal stress and temperature, faults can exhibit either a rate-strengthening behaviour, producing stable sliding, or a rate-weakening behaviour, leading to "stick-slip" motion, (e.g. Dieterich, 1979; Marone, 1998; Ruina, 1983). In the framework of rate-and-state friction, earthquakes can only nucleate in rate-weakening regions, whereas rate-strengthening regions are dominantly characterised by aseismic creep.

However, the complex behaviour of faults not only depends on the frictional properties of the fault interface, but also arises from the effects of static and dynamic stress transfer, levels of pre-stress, and the evolution of the elastic properties of the surrounding medium due to coseismic damage (e.g., Hillers et al., 2006; Kaneko et al., 2010; Kato, 2004; Noda and Lapusta, 2013; Thomas et al., 2017a). For example, although laboratory experiments suggest a rate-strengthening frictional behaviour at shallow depths (Blanpied et al., 1995; Kohlstedt et al., 1995), some active faults seem to be locked near the surface and slip seismically. A striking

* Corresponding author at: Guangdong Provincial Key Laboratory of Geodynamics and Geohazards, School of Earth Sciences and Engineering, Sun Yat-sen University, Guangzhou 510275, China.
E-mail address: zhouyu36@mail.sysu.edu.cn (Y. Zhou).

https://doi.org/10.1016/j.epsl.2017.12.005
0012-821X/

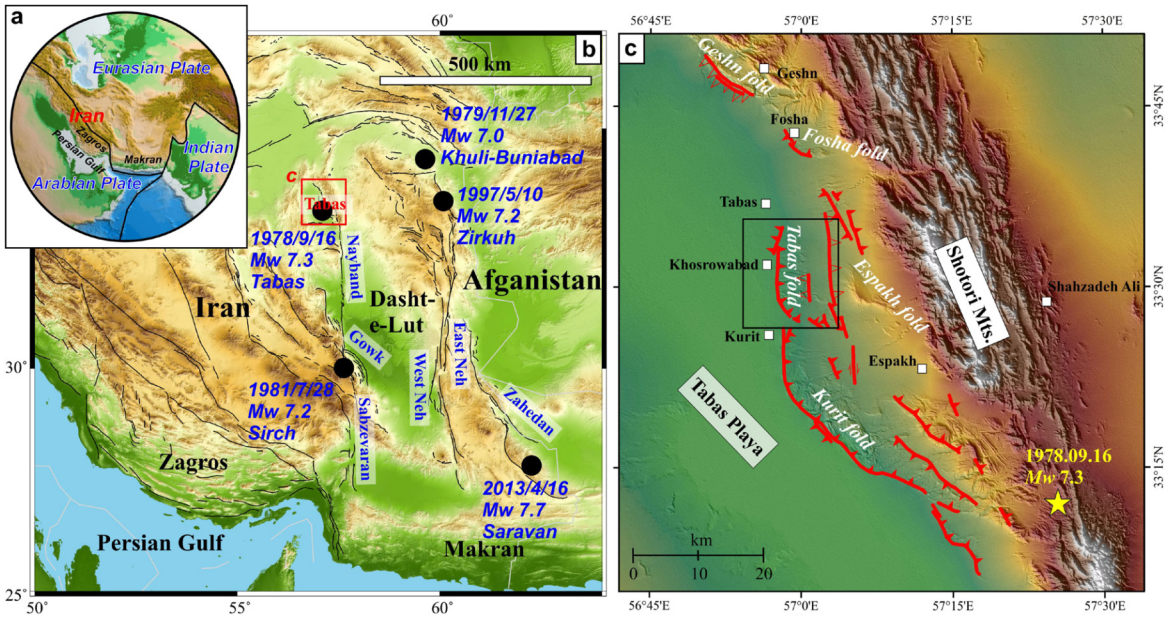

Fig. 1. Tectonic background of the 1978 Tabas-e-Golshan earthquake. (a) Iran is a seismically active country due to the convergence between the Arabian and Eurasian plates. (b) Active faults (black lines) in Iran, from Walker et al. (2003). Black dots are $M_w \geq 7.0$ earthquakes recorded in eastern Iran since 1976, from the GCMT catalogue (Ekström et al., 2012), including the 1978 M_w 7.3 Tabas, 1979 M_w 7.0 Khuli-Buniabad, 1981 M_w 7.2 Sirch, 1997 M_w 7.2 Zirkuh and 2013 M_w 7.7 Saravan earthquakes. (c) Topography of the area inside the box in (b) around Tabas. Surface ruptures (red lines) observed in the field by Berberian (1979). Yellow star indicates the epicentre of the 1978 main shock. Red filled triangles denote thrust faulting and open triangles are high-angle reverse faulting. Black box marks the Tabas fold (Figs. 3–5). (For interpretation of the references to colour in this figure, the reader is referred to the web version of this article.)

case is the 2011 Tohuku-Oki earthquake for which large coseismic slip has been observed on the fault segments that were thought to be rate-strengthening (Noda and Lapusta, 2013). Numerical models suggest that rate-strengthening regions can be locked due to elastic interactions with the adjacent rate-weakening regions, accumulating stresses during the interseismic period, which allows seismic rupture to propagate through them (Kaneko et al., 2010; Thomas et al., 2014b).

To better understand the frictional behaviour of faults in nature, it is necessary to combine laboratory-derived models and geodetic observations of fault slip. In this paper, we use radar interferometry (InSAR) to study the shallow afterslip following the 1978 M_w 7.3 Tabas-e-Golshan earthquake in eastern Iran. Previous studies based on the European Space Agency's (ESA) ERS and Envisat data (Copley, 2014), and optical imagery (Zhou et al., 2016) have found long-lasting afterslip almost 40 yrs after the main shock. The rate was found to decay as $\sim 1/t$ (Zhou et al., 2016). Here, we present deformation time series between 1996 and 2017 derived from ESA's ERS (1996–1999), Envisat (2003–2010) and Sentinel-1A (2014–2017) SAR measurements. The long time series allows us to explore the compatibility of the observed behaviour with what might be expected from laboratory-derived rate-and-state friction laws.

2. Overview of the 1978 Tabas-e-Golshan earthquake

Iran is seismically active due to the convergence between the Arabian and Eurasian plates (Fig. 1a). The convergence rate is estimated to be ~25 mm/yr at longitude 60° (Vernant et al., 2004). Six $M_w \geq 7.0$ earthquakes have been recorded in Iran since 1976 (from the GCMT catalogue) (Ekström et al., 2012), five of which are in the east (Fig. 1b). The 16 September, 1978 Tabas-e-Golshan earthquake (hereafter referred to as the 1978 Tabas earthquake) is the largest (M_w 7.3) and deadliest among them, killing ~11,000 people (Berberian, 1979). It occurred at the northern end of the Nayband fault (Fig. 1b) where north–south right-lateral strike-slip motion turns into a zone of distributed thrusting that is accommodated on a series of folds within Neogene basin deposits (Fig. 1c) (Zhou et al., 2016).

To study the 1978 earthquake, Walker et al. (2003) analysed P and SH seismic waveforms, and found that the main shock occurred on a shallow (16°) dipping thrust with a centroid depth of ~9 km. Applying the fault scaling laws of Scholz (1982), Walker et al. (2003) calculated an average slip of ~3.3 m on the shallow dipping thrust. However, at the surface, the maximum coseismic displacement on the frontal thrust was measured to be only ~35 cm (vertical) at the western margin of the Kurit fold segment (Fig. 1c) (Berberian, 1979). Berberian (1979) also found extensive bedding plane slips along the 85 km-long system of folds (Fig. 1c), with an overall vertical throw of ~1.5 m. Using ERS and Envisat data, Copley (2014) found long-lasting postseismic slip on a steep ramp beneath the Tabas fold (hereafter referred to as the "Tabas ramp") 30 yrs after the main shock. The rate of afterslip was estimated to be ~5 mm/yr in the time interval of 1996–1999 from modelling ERS observations (Copley, 2014).

Recently, Zhou et al. (2016) used both historical and modern optical imagery to measure the surface deformation associated with the 1978 earthquake. Image correlations and DEM differencing revealed a total slip on the ramp of ~7 m on the Tabas ramp between 1978 and 2013, 6.5 m of which occurred between 1978 and 1991. Using their optical measurements and the ERS InSAR rate of Copley (2014) (5 mm/yr between 1996 and 1999), they derived an empirical power law model, $s(t) = 4.4t^{0.02}$, to relate the cumulative afterslip s (metres) and time t (years after the main shock). This simple empirical model shows that the rate of afterslip ($v(t) = \frac{ds}{dt} = 88t^{-0.98}$ mm/yr) decays as $\sim 1/t$, conforming to an "Omori-like decay" of postseismic velocities as discussed by Ingleby and Wright (2017).

Models of fault slip based on both the optical image matching and InSAR results suggest that the Tabas ramp does not reach the surface as a single main fault, but as a distributed zone of deformation from a depth of 0.4 ± 0.2 km (detailed in Section 4). This conforms to the geological observations of the width of the deformation at the surface, i.e. ~220 m wide zone of bedding plane

slip seen in the field (Berberian, 1979) and optical imagery (Zhou et al., 2016). Bedding plane slip is difficult to interpret because the sub-surface motion is not planar, and may therefore be largely "invisible", which creates great challenges to field investigations of earthquake deformation. Nonetheless, they are very common in blind-thrust fault systems. For example, Philip and Meghraoui (1983) found a 200–300 m wide zone of bedding plane slip in the 1980 El-Asnam earthquake (similar to the Tabas earthquake); Berberian et al. (2000) observed significant bedding-plane slip during the 1994 Sefidabeh earthquakes. It is possible, therefore, that field-based studies could have underestimated the coseismic slip of these earthquakes.

In the following sections, we combine geodetic observations and geophysical models, trying to provide a possible means of re-examining the coseismic and postseismic slip of older earthquakes, in this case the 1978 Tabas earthquake.

3. InSAR measurements of postseismic surface deformation

Copley (2014) stacked ERS (1996–1999) and Envisat (2003–2010) interferograms to measure the postseismic deformation. In this paper, we reprocessed the ERS and Envisat data to construct deformation time series. The empirical model of afterslip decay ($v(t) = 88t^{-0.98}$ mm/yr) in Zhou et al. (2016) predicts the rate of afterslip between 2014 and 2017 to be ~2.6 mm/yr. In order to test and improve this empirical model, we also employed Sentinel-1A data to measure the actual rate during this time period. All the interferograms were made and unwrapped using the GAMMA software (Werner et al., 2000). The ERS and Envisat interferograms were multi-looked with a factor of 5 in range and 25 in azimuth, and the Sentinel-1A interferograms with a factor of 20 in range and 4 in azimuth. All the interferograms were resampled to 100 m × 100 m resolution. We discarded interferograms with perpendicular baselines of larger than 300 m (Fig. 2). We then used the Small Baseline Subset (SBAS) method (Berardino et al., 2002) implemented in the Generic InSAR Analysis Toolbox (GIAnT) (Agram et al., 2013) to build the deformation time series.

Note that the deformation time series revealed afterslip on a series of folds that ruptured in the 1978 earthquake (not only the Tabas fold), but here we focus on the Tabas ramp where we can combine the estimates of the total earthquake slip in Zhou et al. (2016) with the InSAR measurements of postseismic rate of slip to investigate the frictional properties of the fault. The InSAR-derived postseismic deformation on other folds has been modelled and discussed by Copley (2014). Note also that the measured surface deformation is insensitive to the motion on the shallow dipping thrust at depth which produces longer wavelength signals (Zhou et al., 2016), so the deformation time series effectively shows just the motion on the ramp.

3.1. ERS: 1996–1999

Although the number of ERS acquisitions (two descending tracks, 435 and 206) was very limited (Fig. 2), fortunately all the interferograms (2 from track 435 and 4 from 206) show a very distinctive tectonic signal across the fault. For ERS track 435, we simply stacked the two interferograms to get the rate map in Fig. 3a. Swath profile A–A′ (2 km wide) shows that the average signal across the fold between 1996 and 1999 in the satellite line-of-sight (LOS) direction is ~2.7 mm/yr (Fig. 3c). For the four interferograms from track 206, we applied empirical (topography-correlated) tropospheric corrections, removed orbital errors, and used the SBAS method to obtain the rate map as shown in Fig. 3b. The average LOS rate is ~ 2.5 mm/yr, similar to that from track 435 and the estimate of Copley (2014) (2.4 mm/yr at roughly the same location, also on track 435).

3.2. Envisat: 2003–2010

We employed 22 acquisitions from Envisat descending track 435, and generated 462 interferograms. For the time series analysis, we selected 43 interferograms (Fig. 2) that show an evident tectonic signal across the fault. After applying atmospheric and orbital corrections, and using the SBAS method, we derived two rate maps (Fig. 4). We separated the Envisat data (2003–2010) into two periods (2003–2005 and 2006–2010) and computed the mean rate between each period in order to see if we could detect small time variations. Swath profile A–A′ in Fig. 4 reveals an average LOS rate of 2.2 mm/yr for 2003–2005, and 1.6 mm/yr for 2006–2010, showing a decrease in rate with time.

3.3. Sentinel-1A: 2014–2017

Sentinel-1A was launched on the 3rd April, 2014; the first image over the Tabas area was acquired in October 2014. We employed 38 acquisitions from descending track 166, and 32 from ascending track 159, over an interval of just over 2 yrs. We formed interferograms by pairwise combination using the COMET InSAR processing software LiCSAR (Spaans et al., 2017), which is built around the GAMMA InSAR software package. It is worth noting that although most Sentinel-1 interferograms have a spatial baseline of less than 100 m, care needs to be taken when using the data because the wider extent of the Sentinel-1 scenes may also result in more "irregular", short-wavelength atmospheric signals within one scene. From our first inspection of the preliminary interferograms, we found that many of the acquisitions were heavily contaminated by atmospheric delays (see Fig. A.10 for an example). The errors are shown by the same fringe patterns in the interferograms with those acquisitions as either the master or slave image. Since we are attempting to measure very small tectonic deformation, we discarded all the contaminated acquisitions in order to minimise the influence of atmosphere. We selected 20 (out of 38) acquisitions from descending track 166 and 21 (out of 32) from track 159 to form the networks in Fig. 2 for time series analysis. Fig. 5 shows the velocity map produced from the time series based on the Sentinel-1A data. Swath profiles in Figs. 5c–d reveal 1.0 mm/yr (descending track 166) and 1.7 mm/yr (ascending track 159) afterslip in the LOS direction between 2014 and 2017. The LOS rate derived from the descending track is smaller than the ascending track because the projections of the east–west and vertical motions, due to slip on the ramp, onto the LOS direction of the descending track are in the opposite sense and will tend to cancel out, whereas for the ascending track, they add.

4. Models of fault slip

The InSAR measurements of surface deformation are in the satellite LOS directions (Figs. 3–5, and Appendix B, Fig. B.11), so in order to compare all the rates of afterslip derived from different satellites and orbital tracks, we need to calculate the slip on the fault plane. To do this, we used an elastic dislocation approach assuming constant slip on a rectangular plane (Okada, 1985). We selected profile A–A′ in the modelling so as to avoid the strong subsidence signal to the north (see Fig. 3), which is possibly caused by groundwater pumping. The free parameters are: slip rate, and the depths to the top and bottom of the fault plane that has slipped. Because we do not have any reference point in the LOS measurements, a linear trend (an offset of the data relative to zero and a gradient along the profile) also needs to be calculated. The strike, dip and rake were fixed to 2°, 50° (Copley, 2014; Zhou et al., 2016) and 90° (i.e. pure thrust motion) respectively. We performed a grid search through the free parameters: varying the slip rate from 0–10 mm/yr in steps of 0.1 mm/yr, and the depth to the

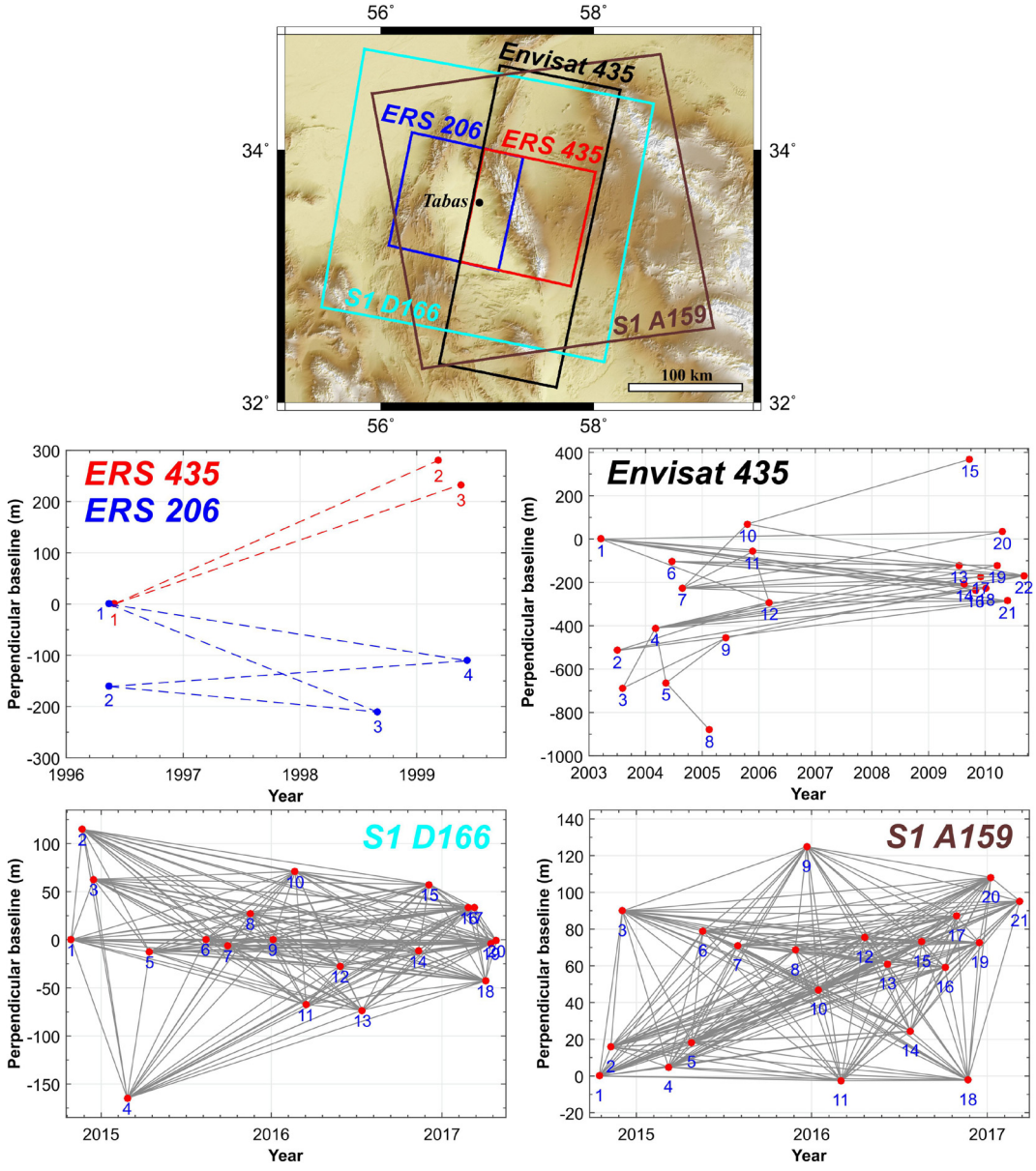

Fig. 2. Baseline plots of selected small baseline interferograms from two ERS tracks (ERS 435 and 206), one Envisat track (Envisat 435) and two Sentinel-1 tracks (S1 D166 and S1 A159). Circles are selected SAR acquisitions: 3 from ERS track 435, 4 from ERS track 206, 22 from Envisat track 435, 20 from Sentinel-1A track 166, and 21 from Sentinel-1A track 159. Lines are the interferograms used in our time-series analysis. Map at top shows coverage for each SAR data set used to derive interferograms.

top of the fault plane from 0–1.0 km in steps of 0.1 km, and the depth to the bottom from 4–10 km in steps of 1 km. We implemented the grid search and computed the residuals between each Okada model and the measured profile. We fitted a linear trend to the residuals and removed it from the measured profile, and then recalculated the residuals between the Okada models and the new profile. The procedure was undertaken for all the profiles shown in Figs. 3–5. The solutions with the minimum misfit (the standard deviation of the residuals, RMSE) are shown in Fig. 6 with the parameters listed in Table 1.

All the best-fitting models in Table 1 gave a bottom depth of 5 ± 1 km, consistent with 4–5 km in Copley (2014) and 6 km in Zhou et al. (2016). The top depth, 0.4 ± 0.2 km, although slightly larger than 0.1 km in Zhou et al. (2016), confirms that the deformation is distributed near the surface (Zhou et al., 2016). There is some trade-off between the fault depths and slip rates, but since we have prior estimates of the likely depths from our previous study and the wavelength of the deformation signal, the slip rates are well constrained in the inversions. The ERS rates between 1996 and 1999 from different tracks, 5.0 ± 0.8 mm/yr (ERS D435) and 4.2 ± 0.5 mm/yr (ERS D206), agree well with the estimate by Copley (2014) (5 ± 1 mm/yr). The afterslip rate shows an evident decrease from ~4.5 mm/yr in 1996–1999, to a present rate of ~2.5 mm/yr.

Based on the empirical model of afterslip decay ($v(t) = 88t^{-0.98}$ mm/yr) from Zhou et al. (2016), we can calculate the average afterslip rate in 2003–2005 (3.6 mm/yr), 2006–2010 (3.1 mm/yr), and 2014–2017 (2.6 mm/yr) respectively. These estimates are solely based on the optical image matching results of Zhou et al. (2016) and the ERS measurements of Copley (2014), and are therefore independent of the Envisat and Sentinel-1A measurements. Nonetheless, we found good agreement between them: 3.6 mm/yr (predicted) versus 3.9 mm/yr (measured) in 2003–2005, 3.1 mm/yr (predicted) versus 3.0 mm/yr (measured) in 2006–2010, and 2.6 mm/yr (predicted) versus 2.7 (and 2.3) mm/yr (measured) in 2014–2017.

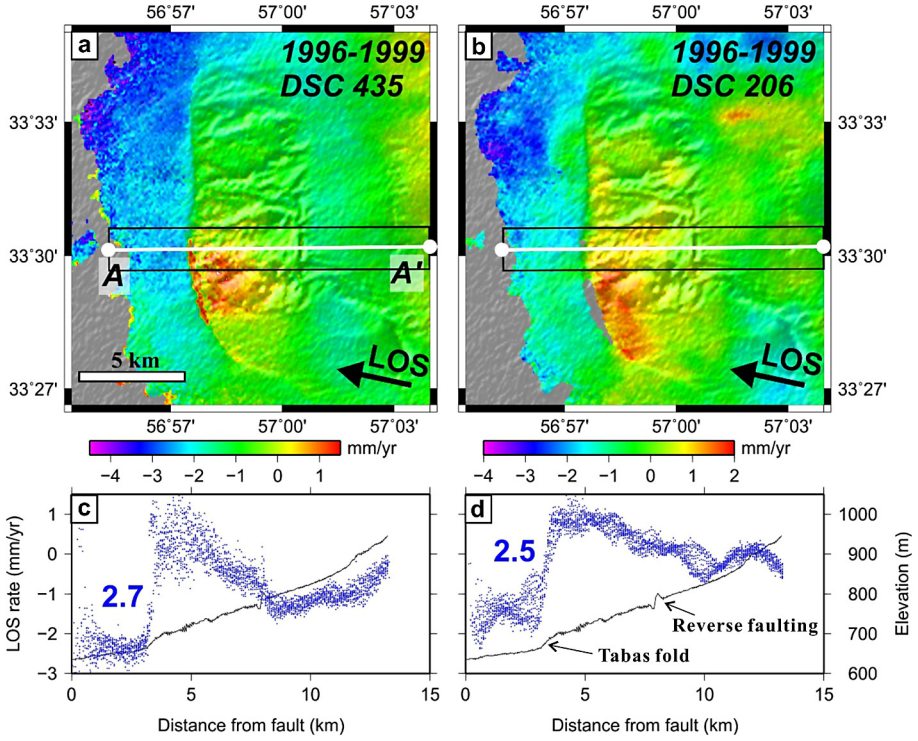

Fig. 3. Average LOS velocity between 1996 and 1999 from time series of ERS interferograms. The satellite LOS direction is shown by the black arrow marked "LOS". See Fig. 1c for location. (a) Rate map derived from ERS track 435. (b) Rate map derived from ERS track 206. (c) and (d) Swath profiles (black box, 2 km wide) of motions (blue points) and topography (black lines, from SPOT-6 DEM (Zhou et al., 2016)) along A–A′. The average amplitude of LOS rates is estimated to be 2.7 mm/yr and 2.5 mm/yr for tracks 435 and 206 respectively. Positive rates indicate motion towards the satellite. The topographic profile reveals two long-term features: at ∼4 km, the change in elevation is due to long-term thrusting on the Tabas fold; at ∼8 km, the topographic variation is associated with high-angle reverse faulting on the structure as shown in Fig. 1. (For interpretation of the references to colour in this figure, the reader is referred to the web version of this article.)

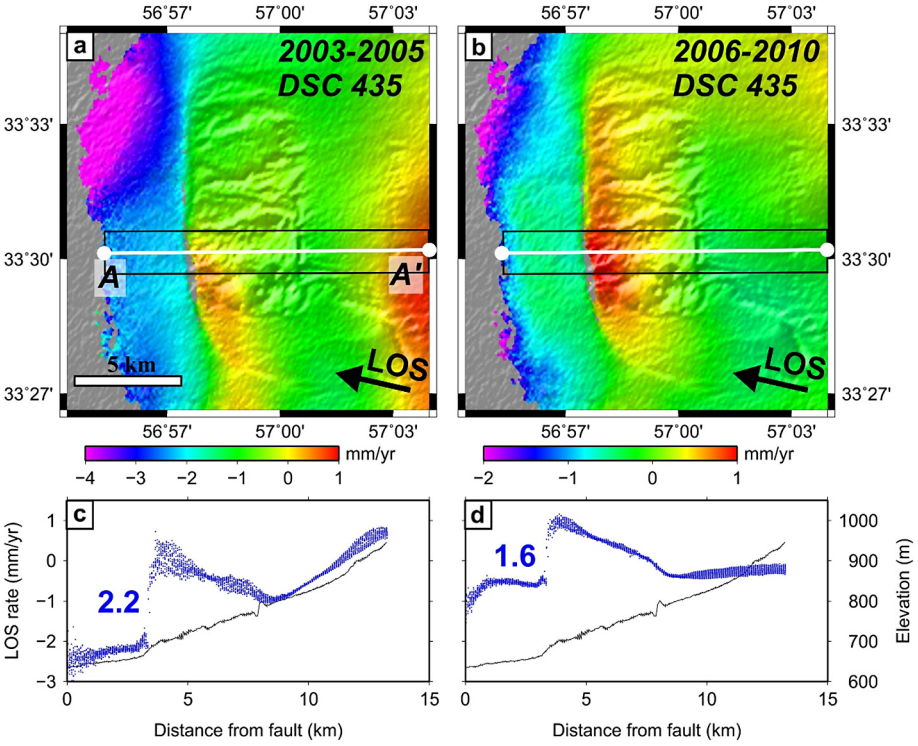

Fig. 4. Average LOS velocity between 2003 and 2010 from time series of Envisat interferograms. The satellite LOS direction is shown by the black arrow marked "LOS". See Fig. 1c for location. (a) Average LOS velocity between 2003 and 2005. (b) Average LOS velocity between 2006 and 2010. (c) and (d) Swath profiles (black box, 2 km wide) of rate of LOS displacement (blue points) and topography (black lines) along A–A′. The average amplitude of LOS rates is estimated to be 2.2 mm/yr and 1.6 mm/yr for 2003–2005 and 2006–2010 respectively. Positive rates indicate motion towards the satellite. (For interpretation of the references to colour in this figure, the reader is referred to the web version of this article.)

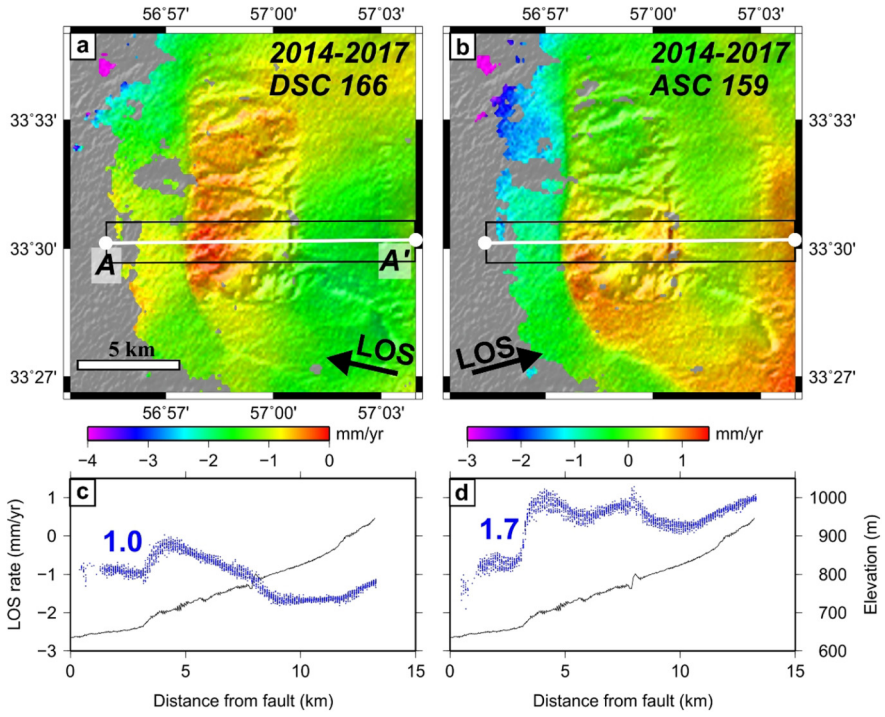

Fig. 5. Average LOS velocity between 2014 and 2017 from time series of Sentinel-1A interferograms. The satellite LOS direction is shown by the black arrow marked "LOS". See Fig. 1c for location. (a) Rate map derived from Sentinel-1A descending track 166. (b) Rate map derived from Sentinel-1A ascending track 159. (c) and (d) Swath profiles (black box, 2 km wide) of motions (blue points) and topography (black lines) along A–A′. The average amplitude of LOS rates is estimated to be 1.0 mm/yr and 1.7 mm/yr for descending track 166 and ascending track 159 respectively. Positive rates indicate motion towards the satellite. (For interpretation of the references to colour in this figure, the reader is referred to the web version of this article.)

5. Analysis and discussion

In this section, we combine our InSAR time series of afterslip and the image matching results of the earthquake and postseismic slip of Zhou et al. (2016) to investigate the "rate-and-state" nature of friction on the Tabas ramp.

5.1. Rate-and-state friction laws and analytical solutions

Laboratory-derived rate-and-state friction laws (Dieterich, 1979; Marone, 1998; Ruina, 1983) have been extensively used to reproduce fault slip behaviour (e.g., Avouac, 2015; Hillers et al., 2006; Kato, 2004; Noda and Lapusta, 2013; Perfettini and Avouac, 2004; Thomas et al., 2017b). Here we adopt the friction law, including the effect of aging, proposed by Dieterich (1979) and Ruina (1983):

$$\tau_f = \bar{\sigma}\left[\mu_* + a\ln\left(\frac{V}{V_*}\right) + b\ln\left(\frac{\theta V_*}{D_c}\right)\right] \tag{1}$$

$$\frac{d\theta}{dt} = 1 - \frac{V\theta}{D_c} \tag{2}$$

where τ_f is the shear stress, $\bar{\sigma}$ is the effective normal stress, V is the slip rate, V_* is the reference slip rate, μ_* is the coefficient of friction for $V = V_*$ in the steady state, θ is the state variable, D_c is the critical slip for state variable evolution, and $a > 0$ and $b > 0$ are the constitutive parameters. At constant velocity, θ evolves to its steady state value D_c/V so that $\frac{d\theta}{dt} = 0$, and the shear stress τ_f depends purely on the slip rate:

$$\tau_f = \bar{\sigma}\left[\mu_* + (a-b)\ln\left(\frac{V}{V_*}\right)\right] \tag{3}$$

Hence, the value of the parameter combination $a - b$ defines the fault behaviour at steady state: $a - b > 0$ corresponds to rate-strengthening friction properties, leading to stable slip with the imposed loading rate, whilst $a - b < 0$ defines potentially seismic, rate-weakening fault behaviour.

Considering the fault as a spring-slider system (Fig. 7), Perfettini and Avouac (2004) derived analytical solutions for estimating the rate-and-state frictional parameters. In the spring-slider model, there is a force balance between the frictional stress $\tau_f(V)$ and the sum of the elastic and applied stresses:

$$\tau_f(V) = \tau_i + k(V_0 t - \delta) + \Delta\tau_c \tag{4}$$

where τ_i is the initial stress, k is the spring stiffness, V_0 is the long-term slip rate, t is time, δ is the slip of the block, and $\Delta\tau_c$ is the applied stress due to earthquakes, i.e. the Coulomb stress change $\Delta\tau_c = \Delta\tau - \mu_*\Delta\sigma$ (with the geomechanical convention that normal stress is positive in compression and the friction coefficient μ approximated as μ_*).

At $t = 0$, the initial rate V_i (i.e. the preseismic slip rate) leads to

$$\tau_f(V_i) = \tau_i - k\delta_i \tag{5}$$

where δ_i is the initial slip. Hence, we have:

$$\tau_f(V) - \tau_f(V_i) = k(V_0 t - U) + \Delta\tau_c \tag{6}$$

where $U = \delta - \delta_i$ is the afterslip.

Combining Equations (3), i.e. assuming the frictional stress is given by the steady-state relationship, and (6), we obtain:

$$(a-b)\bar{\sigma}\ln\left(\frac{V}{V_i}\right) = k(V_0 t - U) + \Delta\tau_c \tag{7}$$

Re-arranging Equation (7) gives an equation relating slip rate to slip:

$$\frac{dU}{dt} = V_i \exp\left[k\frac{V_0 t - U}{(a-b)\bar{\sigma}} + \frac{\Delta\tau_c}{(a-b)\bar{\sigma}}\right] \tag{8}$$

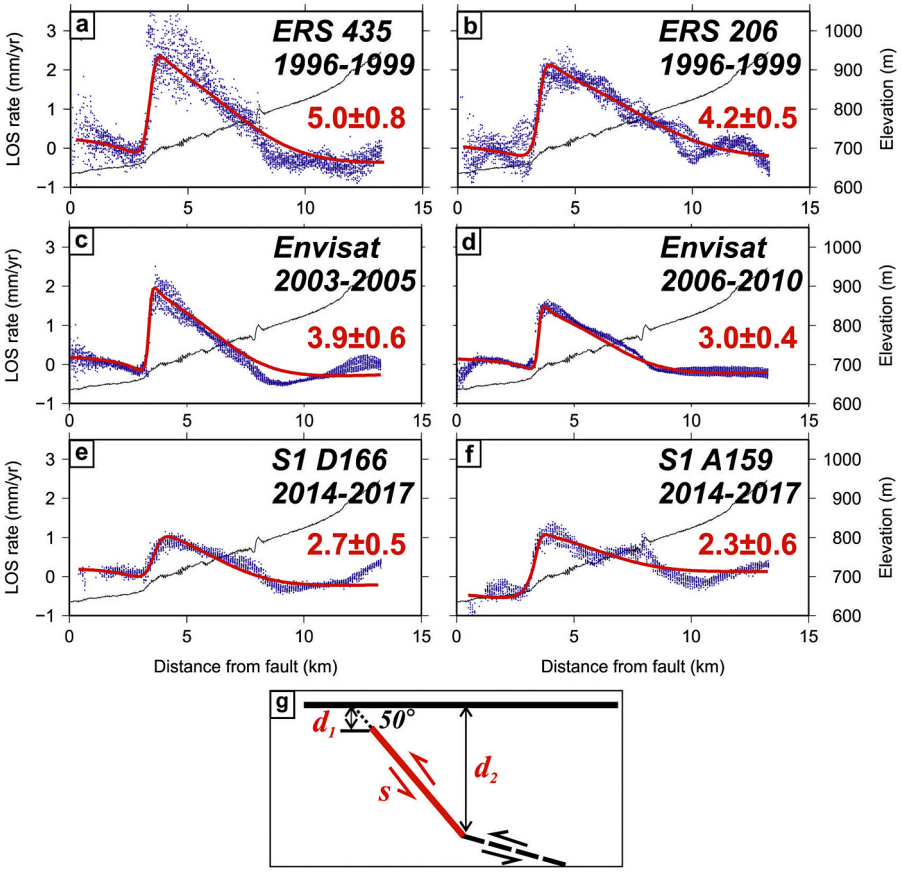

Fig. 6. Models of fault slip that best fit the ground motion (red) measured using SAR data (blue points) from (a) ERS track 435 (1996–1999), (b) ERS track 206 (1996–1999), (c) Envisat track 435 (2003–2005), (d) Envisat track 435 (2006–2010), (e) Sentinel-1A track 166 (2014–2017), and (f) Sentinel-1A track 159 (2014–2017). The model parameters are listed in Table 1. (g) Sketch of fault geometry. The observed surface deformation is due to motion on the ramp (red solid line). We invert for the top and bottom depths (d_1 and d_2 respectively) and slip (s) in the modelling. (For interpretation of the references to colour in this figure, the reader is referred to the web version of this article.)

Table 1
Details of the grid search parameters that best fit the InSAR data. See text for descriptions.

Modelling of InSAR measurements						
Parameters	ERS D435	ERS D206	Envisat D435		S1 D166	**S1 A159**
	(1996–1999)	(1996–1999)	(2003–2005)	(2006–2010)	(2014–2017)	(2014–2017)
Incidence (°)	28.7	21.0	25.7		39.0	36.0
Heading (°)	−166	−166	−168		−167	−13
Slip rate (mm/yr)	5.0 ± 0.8	4.2 ± 0.5	3.9 ± 0.6	3.0 ± 0.4	2.7 ± 0.5	2.3 ± 0.6
Depth to top (km)	0.4	0.4	0.2	0.2	0.6	0.4
Depth to bottom (km)	5	6	4	4	4	5
Location (km)[1]	3.3	3.5	3.4	3.4	3.6	3.5
Gradient (mm/yr/km)[2]	0.193	0.126	−0.0258	0.0548	−0.0489	0.0928
Offset (mm/yr)[3]	−2.88	−1.57	−2.87	−0.705	−0.923	−0.56

Models in Zhou et al. (2016)			
Parameters	Optical image matching		DEM differencing
	(1974–1991)	(1974–2013)	(1956–2013)
Slip (m)[4]	6.5 ± 0.5	7.0 ± 0.5	7.0 ± 0.5
Depth to top (km)	0.1	0.1	0.1
Depth to bottom (km)	6	6	6

[1] The along-profile position of the projection of the fault plane onto the surface.
[2] Velocity gradient along the profile.
[3] Offset of the measurements relative to zero.
[4] The estimated slip is a combination of coseismic and postseismic motion.

In Equation (8), the input parameters are: the constitutive parameter $(a-b)$, the equivalent stiffness k, the static Coulomb stress change $\Delta\tau_c$ induced by the coseismic event at time $t=0$, the long-term slip rate V_0, and the pre-seismic slip rate V_i.

Integrating Equation (8), Perfettini and Avouac (2004) obtained the solution:

$$U(t) = \alpha \ln\left[1 + \frac{\beta V_i}{V_0}\left(\exp\left(\frac{t}{t_r}\right) - 1\right)\right] \tag{9}$$

where

$$\alpha = \frac{(a-b)\bar{\sigma}}{k} \tag{10}$$

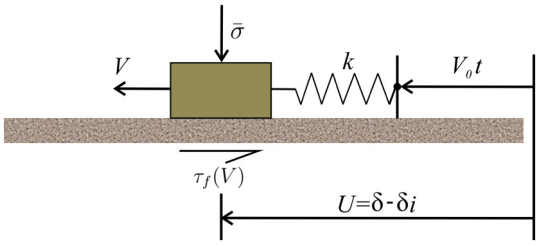

Fig. 7. Spring-slider model used to derive the analytical solutions for the afterslip on the Tabas ramp. The system is pushed from the right. See Section 5.1 for notation.

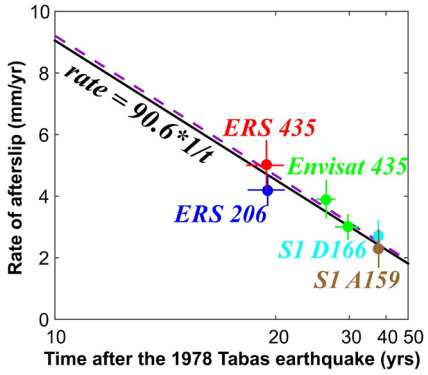

Fig. 8. Rates of afterslip decay as $\sim 1/t$. Coloured dots are InSAR-derived rates, with short lines indicating the uncertainties in both rate and time. Black line is the best-fitting model to the measurements. The gradient, i.e. α (defined in Section 5), is 90.6 mm. Purple dashed line is the empirical model of afterslip decay $v(t) = 88t^{-0.98}$ from Zhou et al. (2016). (For interpretation of the references to colour in this figure, the reader is referred to the web version of this article.)

$$t_r = \frac{\alpha}{V_0} \tag{11}$$

$$\beta = \exp\left(\frac{\Delta\tau_c}{(a-b)\bar{\sigma}}\right) \tag{12}$$

The parameter α corresponds to the characteristic length scale over which the elastic stress changes by order of the frictional stress; t_r is a characteristic relaxation time determined by the characteristic length scale α and long-term slip rate V_0; β is a scaling factor by which the sliding rate increases or decreases in response to the applied stress $\Delta\tau_c$. Therefore, βV_i is the initial rate at the beginning of the postseismic period. In a rate-strengthening area with $a - b > 0$, positive $\Delta\tau_c$ will induce an increase in the sliding rate V_i by β.

Taking the derivative of $U(t)$ with respect to time t, we obtain the rate of afterslip:

$$V(t) = \beta V_i \frac{\exp\left(\frac{t}{t_r}\right)}{1 + \frac{\beta V_i}{V_0}\left(\exp\left(\frac{t}{t_r}\right) - 1\right)} \tag{13}$$

Assuming $\frac{\beta V_i t}{\alpha} \gg 1$ and $t < t_r$, using a Taylor series expansion of $\exp\left(\frac{t}{t_r}\right)$, and neglecting higher-order terms, we can simplify Equations (9) and (13):

$$U(t) \approx \alpha \ln\left[1 + \frac{\beta V_i t}{\alpha}\right] \tag{14}$$

$$V(t) \approx \frac{\alpha}{t} \tag{15}$$

5.2. Afterslip rate and coseismic slip

The measured rates are plotted versus $1/t$ in Fig. 8. Using a weighted least-squares adjustment, we solved for the best-fitting line, obtaining a value for α of 90.6 mm. The InSAR measurements show good agreement with the relationship $V(t) = \frac{90.6}{t}$ mm/yr. However, we also have an estimate of the slip that occurred in 1978–1991 (6.5 m in 13 yrs) and 1978–2013 (7.0 m in 35 yrs) (Table 1), and we can use these values to calculate the other parameters in Equation (14). Note that the slip estimates are the total slip, i.e. a combination of coseismic (U_{CS}) and postseismic ($U_{POST}(t)$) motion. For simplicity we made the assumption that no significant preseismic slip occurred, which is probably true since the slip measurements between 1956–2013 and 1974–2013 are consistent (Table 1). Therefore:

$$U_{CS} + U_{POST}(1978{-}1991) = 6.5 \pm 0.5\,\text{m} \tag{16}$$

$$U_{CS} + U_{POST}(1978{-}2013) = 7.0 \pm 0.5\,\text{m} \tag{17}$$

Based on Equations (14), (16) and (17), we can estimate parameters U_{CS} and βV_i. The best-fit solutions gave $U_{CS} = 5.8$ m and $\beta V_i = 3.5 \times 10^{-6}$ m/s. Note that the estimate of α depends solely on the decay of the afterslip rate, i.e. the InSAR measurements, and is independent of the total slip estimates.

Because the optical image matching results contain relatively larger errors compared to InSAR, we also tried different combinations of U_{CS} and βV_i. To do so, we varied U_{CS} from 0–7 m and computed βV_i. Fig. 9 shows that a series of values for U_{CS} and βV_i can fit the observations reasonably well, with βV_i decreasing rapidly as U_{CS} increases (Fig. 9b). Because βV_i corresponds to the initial rate at the beginning of the postseismic period, it cannot exceed the coseismic slip rate, which is on the order of 1 m/s. Therefore, in order to get a physically meaningful value of βV_i, the coseismic slip has to be at least ~4.7 m.

The modelled coseismic slip (~5 m) appears to be large given that this amount of slip is not observed at the surface. Nonetheless, we know that there was extensive bedding plane slip over a wide zone, suggesting that the near-surface (above a depth of ~0.4 km) deformation is distributed over a zone of similar width. The apparent vertical throw measured in the field (a minimum of 1.5 m summed across multiple bedding planes) (Berberian, 1979) is possibly bedding-plane shear driven by the coseismic slip at depth.

It is interesting to note how fast afterslip could occur just after the earthquake (Fig. 9). Using the lower bound of the coseismic slip (~4.7 m), rate-and-state friction laws using Equation (14) predict ~1.1 m afterslip in 0.5 days immediately after the main shock, which is ~60% of the total afterslip (1.8 m). This raises some concerns about using InSAR and optical images to measure coseismic deformation. Since the first post-earthquake image is usually acquired a few days after an event, "coseismic displacements" derived from InSAR and optical images may contain a significant amount of afterslip in some cases. In the 2004 Parkfield earthquake, Langbein et al. (2006) analysed the very early GPS data, and found that 1 day after the earthquake, the postseismic creep (2.5 cm) could be as much as the coseismic displacement (2.5 cm) at some stations.

To calculate the characteristic relaxation time t_r, we use a long-term geological loading rate on the fault of $V_0 = 1.5$ mm/yr. We do not have any direct measurements of V_0. The value was estimated assuming that the long-term thrusting on the Tabas fault accommodates the right-lateral strike-slip on the Nayband fault to its south. The ~1.5 mm/yr strike-slip on the Nayband fault (Foroutan et al., 2014; Walker et al., 2009) would result in ~1.0 mm/yr shortening on the Tabas fault, thereby ~1.5 mm/yr slip on the Tabas ramp given a fault dip of 50°. The relaxation time $t_r = 60.4$ yrs, though much larger than the typical value of 7–11 yrs (Perfettini and Avouac, 2004), is not surprising given the long timescale of the observed afterslip.

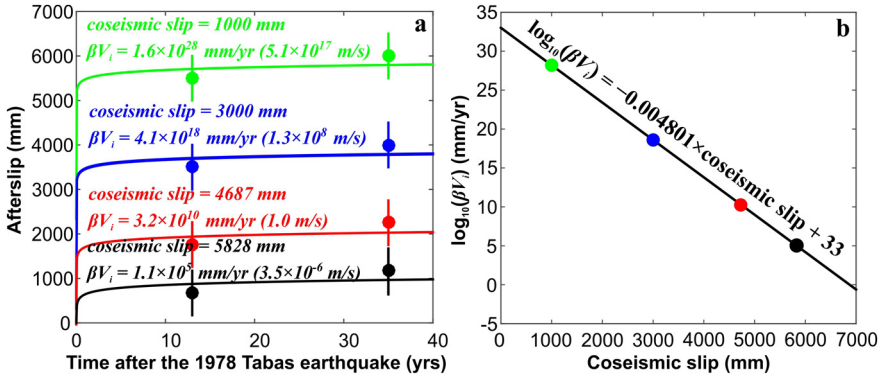

Fig. 9. (a) Estimates of afterslip based on different combinations of assumed coseismic slip and βV_i. Coloured dots are the optical measurements, with coloured lines showing the best-fitting models. (b) The best-fitting parameter βV_i is inversely proportional to the assumed coseismic slip. See Section 5.3 for details.

5.3. Frictional properties of the Tabas ramp

We used our InSAR measurements of afterslip on the Tabas ramp to estimate the frictional properties of the fault by applying two slightly different methods.

In the first method, we make some assumptions about the elastic properties of the medium. Based on Equation (10), we estimated the constitutive parameter $(a-b)\bar{\sigma} = 0.18$ MPa for an equivalent stiffness of $k = G/h$, where $G = 10$ GPa is the shear modulus of the medium near the surface and $h = 5$ km corresponds to the thickness of the rate-strengthening region (i.e. the bottom depth of the Tabas ramp). The friction parameter $(a-b)$ can then be computed if the effective normal stress is known. The distribution of effective normal stress $\bar{\sigma}$ with depth is usually calculated by assuming hydrostatic pore pressure and a rock density of 2700 kg/m^3 (a typical value for the continental crust). This leads to $\bar{\sigma} \approx 50$ MPa for a representative depth value on the ramp ($z = 3$ km) and consequently to $(a-b) = 0.0036$.

In the second method, we start from the static Coulomb stress change induced by the coseismic event. Using a simple fault geometry that follows the surface trace and takes into account the change in fault dip at 5 km depth, we estimate how much coseismic slip must have occurred on the detachment to get a M_w 7.3 earthquake if the ramp has slipped 4.7 m. Assuming uniform slip over the entire 80 km fault length (extending to 12 km at depth), with 4.7 m slip on the 50° dipping ramp from a depth of 0.1–5 km, yields a slip of 1.7 m on the 16° dipping detachment, much smaller than the ≥ 4.7 m required to drive postseismic creep on the Tabas ramp, and also smaller than that estimated by Walker et al. (2003). However, as more coseismic surface ruptures (Berberian, 1979) and postseismic deformation (Copley, 2014) were observed in the north than the south, we suspect that, although the entire 80 km length ruptured, the amount of slip varied along fault strike, with the maximum at the latitude of the Tabas fold. Taking the extreme case, where coseismic slip was concentrated in the northern segment of the fault (i.e. the Tabas fold) with homogeneous slip on the ramp and the detachment, we obtained a coseismic slip of 7.1 m on the detachment in order to have a M_w 7.3 earthquake. We then used the Coulomb3 software (Lin and Stein, 2004) to compute the Coulomb stress change on the ramp induced by the motion on the detachment, and obtained $\Delta\tau_c = 3.5$ MPa. For a coseismic slip of 4.7 m, we have $\beta = 2.1 \times 10^{10}$ (given $\beta V_i = 3.2 \times 10^{10}$ mm/yr as shown in Fig. 9a, and the long-term geological slip rate $V_i = 1.5$ mm/yr). Based on Equation (12), we can estimate the constitutive parameter $(a-b)\bar{\sigma} = 0.15$ MPa. Using the same estimate of the effective normal stress as described above, we inferred $a-b = 0.0029$ on the ramp, which leads to an equivalent stiffness of $k = 1.6 \times 10^6$, of the same order in magnitude as the value we inferred for the first method ($k = 2 \times 10^6$).

The estimates of $a-b$ from the two different methods are consistent, which lends confidence to the results. Both values, $a-b = 0.0036$ and $a-b = 0.0029$, fall in the range of laboratory-derived values for various rock types with rate-strengthening properties (between 10^{-3} and 10^{-2}) (Marone, 1998). They are also compatible with those from other studies, e.g. 0.0066 after the 2003 Chengkung earthquake (Chang et al., 2009), and 0.002 along the creeping section of the Haiyuan fault (Jolivet et al., 2013). Our $a-b$ is small, close to velocity neutral, which may allow seismic rupture to propagate through the fault segment.

5.4. Possible mechanisms for the overlap of seismic and postseismic slip

The geodetic studies of the 1978 Tabas-e-Golshan earthquake and the postseismic slip that followed suggest that both coseismic slip and afterslip occurred on the ramp, i.e. at the same location. Although this phenomenon appears controversial, it has been inferred for other earthquakes, such as the 2003 Chengkung (Thomas et al., 2017b) and 2010 Maule earthquakes (Bedford et al., 2013). Here, we discuss the possible mechanisms that can explain such behaviour.

The first hypothesis is to assume that the frictional properties we infer for the Tabas ramp are stable throughout the entire seismic cycle and therefore, that the dynamic rupture during the 1978 Tabas-e-Golshan earthquake propagates into a rate-strengthening region. Numerical models of earthquake sequences based on rate-and-state friction laws have suggested that, for high pre-level of stress and/or for small positive values of the frictional parameter $a-b$, dynamic rupture may propagate across a rate-strengthening region (Kaneko et al., 2010; Thomas et al., 2014b). Our inferred values of $a-b = 0.0036$ or $a-b = 0.0029$ are consistent with these models. Based on the study of Thomas et al. (2014b), for a 5-km-long segment with $a-b = 0.003$ there is a ~80% chance that an earthquake propagates through the rate-strengthening region. Moreover, at seismic slip rates (~ 1 m/s), laboratory experiments have shown that the dynamic coefficient of friction may drop drastically (e.g., Di Toro et al., 2011; Wibberley et al., 2008), which then enhances seismic propagation in rate-strengthening areas. Additional friction weakening mechanisms advocated to explain such behaviour are related to shear heating that unavoidably occurs during fast sliding that accumulates significant slip. The first mechanism, described as "flash heating", has both theoretical and experimental support (e.g., Goldsby and Tullis, 2011; Rice, 2006; Tsutsumi and Shimamoto, 1997). During seismic faulting, fault gouge grains heat up at asperity contacts and substantially weaken. Pore fluid pressurisation is another shear-heating-related weakening mechanism that might take place during seismic slip (e.g., Rice, 2006; Sibson, 1973). In that case, pore fluid expands faster in the shearing layer than the surrounding porous space,

which increases the pore fluid pressure and hence decreases the effective normal stress. Other weakening processes, including frictional melting (e.g., Hirose and Shimamoto, 2005; Tsutsumi and Shimamoto, 1997) and gel formation (e.g., Goldsby and Tullis, 2002) have also been suggested.

Another hypothesis is to assume that the frictional properties of the fault interface vary with time. This idea has been explored theoretically by Thomas et al. (2017b), who proposed that the overlap of coseismic and postseismic slip may occur by shear-heating-induced transient change of rate-and-state properties. The dependence of quasi-static (slow-rate) friction properties on bulk temperature has been well-established (e.g., Blanpied et al., 1995; den Hartog et al., 2012; Verberne et al., 2014). Typically, at high enough temperatures, the rate-and-state properties can transit from rate-weakening to rate-strengthening. Thomas et al. (2017b) hypothesise that such a transition from rate-weakening to rate-strengthening can also transiently occur within a rate-weakening region due to coseismic shear heating. For this particular scenario, it would mean that, before the 1978 Tabas-e-Golshan earthquake, the properties of the ramp were rate-weakening, which explains the large coseismic slip inferred. The (rapid) coseismic shear heating would have then triggered a change in the properties of the fault interface leading to a rate-strengthening behaviour. If the overall Coulomb stress changes due to the coseismic rupture are positive, this could trigger afterslip on the ramp. Over time, temperature evolves through off-fault diffusion of heat and the rate-and-state parameter $a - b$ slowly changes accordingly towards its preseismic rate-weakening value.

Both scenarios are plausible. However, as the temperature change between now (almost 40 yrs after the main shock) and before the earthquake would be too small (probably less than 1°C) to change $a - b$ significantly, the second hypothesis is unlikely to be the true explanation. It is more likely that the frictional properties of the Tabas ramp remain rate-strengthening through the entire seismic cycle, with the frictional parameter $a - b$ being close to zero, favouring earthquake propagation.

6. Conclusions

We have investigated the postseismic deformation along the Tabas fold segment after the 1978 M_w 7.3 Tabas earthquake using over 20 yrs of ESA's InSAR data. The deformation time series shows a $\sim 1/t$ decay in postseismic velocities from 5.0 $\pm$ 0.8 mm/yr in 1996–1999 to 3.9 $\pm$ 0.6 mm/yr in 2003–2005, 3.0 $\pm$ 0.4 mm/yr in 2006–2010, and a present rate of 2.3 $\pm$ 0.6 mm/yr in 2014–2017. Combining the InSAR rates and the estimates of the total earthquake slip made by Zhou et al. (2016), we analysed the frictional properties of the Tabas ramp fault using the rate-and-state friction framework. The rate-and-state parameter $a - b \approx 0.003$ indicates rate-strengthening frictional behaviour. We also inferred a coseismic slip of $\geq$4.7 m (rate-weakening) at the same location. This phenomenon, where coseismic slip overlaps with postseismic slip, appears controversial, but it has been observed in other places, e.g. the 2003 Chengkung (Thomas et al., 2017b) and 2010 Maule earthquakes (Bedford et al., 2013). One possible mechanism is that the frictional parameter $a - b$ is small enough (close to velocity neutral) to allow dynamic ruptures to propagate in rate-strengthening regions (Kaneko et al., 2010; Thomas et al., 2014b). The other possibility is that preseismic rate-weakening behaviour may transit to postseismic rate-strengthening due to coseismic shear heating (Thomas et al., 2017b). In the case of the 1978 Tabas earthquake, because we are still seeing afterslip almost 40 yrs following the main shock, the Tabas ramp is more likely to be rate-strengthening throughout the entire seismic cycle. However, although rate-strengthening, there is a high chance (~80%) for earthquakes to propagate onto the ramp since the frictional parameter $a - b$ is small.

Acknowledgements

This work was supported by the Natural Environment Research Council through the Looking into the Continents from Space (LiCS) large grant (NE/K011006/1), the NERC/ESRC Earthquakes without Frontiers (EwF) consortium and the Centre for the Observation and Modelling of Earthquakes, Volcanoes and Tectonics (COMET). The SAR data were provided by the European Space Agency (ESA). Figures were prepared using the Generic Mapping Tools software (Wessel and Smith, 1998). We thank Tim Wright, Alex Copley and Yann Klinger for discussions about postseismic creep, and earthquake physics and geology in general. We also thank Philippe Vernant and an anonymous reviewer for their useful comments.

Appendix A. Atmospheric errors in Sentinel-1 interferograms

Although the extent of the Sentinel-1 scenes is wider, it may also result in more "irregular", short-wavelength atmospheric signals within one scene. For example, in Fig. A.10, the interferograms

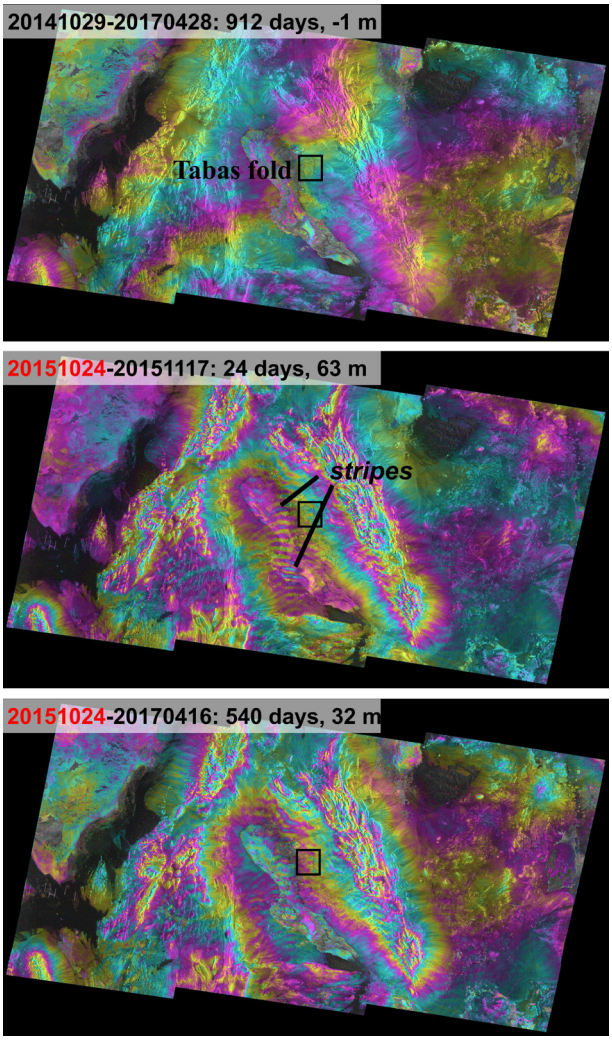

Fig. A.10. Examples of atmospheric errors in Sentinel-1 interferograms. The top interferogram is a "clean" one that mainly contains long-wavelength orbital ramps. The middle and bottom interferograms are contaminated by the atmospheric errors (stripes) in the acquisition 20151024 (labelled in red). Black box indicates the Tabas fold. (For interpretation of the references to colour in this figure, the reader is referred to the web version of this article.)

with the same acquisition (20151024) as the master image show some stripes, which are due to atmospheric effects. The interferogram 20141009-20170428 is "clean"; the long-wavelength signals do not affect our measurements of short-wavelength tectonic signal. We only used these "clean" acquisitions to form interferograms.

Appendix B. Rate maps

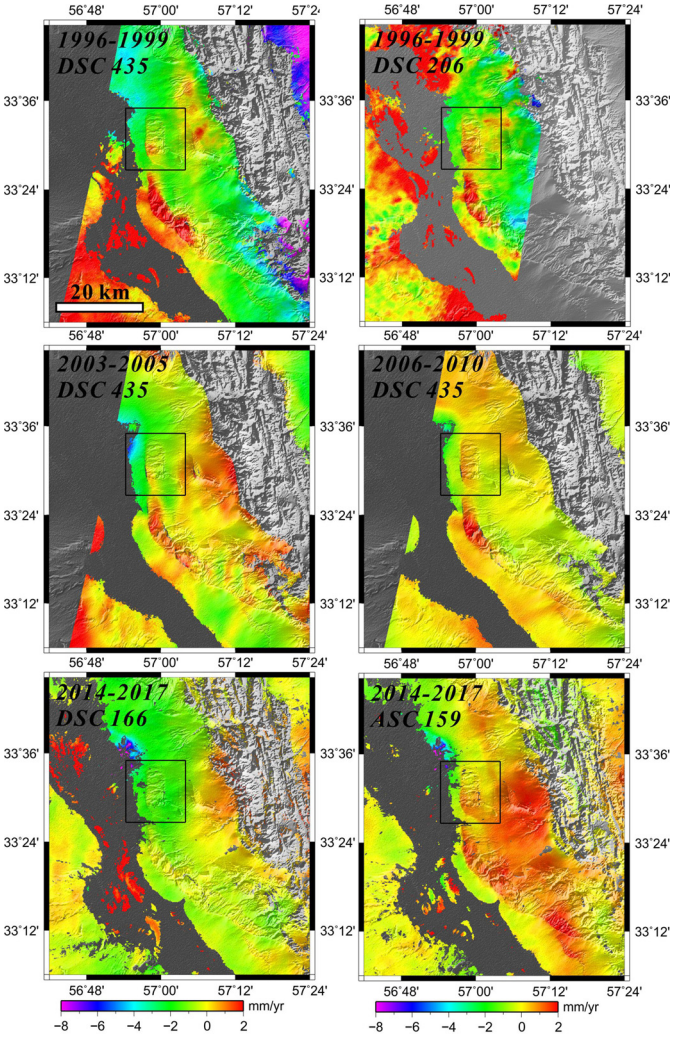

Fig. B.11. Rate maps derived from ERS, Envisat and Sentinel-1 data. Black box marks the coverage of Figs. 3–5.

References

Agram, P., Jolivet, R., Riel, B., Lin, Y., Simons, M., Hetland, E., Doin, M.-P., Lasserre, C., 2013. New radar interferometric time series analysis toolbox released. Eos 94 (7), 69–70.

Avouac, J.-P., 2015. From geodetic imaging of seismic and aseismic fault slip to dynamic modeling of the seismic cycle. Annu. Rev. Earth Planet. Sci. 43, 233–271.

Bedford, J., Moreno, M., Baez, J.C., Lange, D., Tilmann, F., Rosenau, M., Heidbach, O., Oncken, O., Bartsch, M., Rietbrock, A., Tassara, A., Bevis, M., Vigny, C., 2013. A high-resolution, time-variable afterslip model for the 2010 Maule Mw = 8.8, Chile megathrust earthquake. Earth Planet. Sci. Lett. 383, 26–36.

Berardino, P., Fornaro, G., Lanari, R., Sansosti, E., 2002. A new algorithm for surface deformation monitoring based on small baseline differential SAR interferograms. IEEE Trans. Geosci. Remote Sens. 40 (11), 2375–2383.

Berberian, M., 1979. Earthquake faulting and bedding thrust associated with the Tabas-e-Golshan (Iran) earthquake of September 16, 1978. Bull. Seismol. Soc. Am. 69 (6), 1861–1887.

Berberian, M., Jackson, J., Qorashi, M., Talebian, M., Khatib, M., Priestley, K., 2000. The 1994 Sefidabeh earthquakes in eastern Iran: blind thrusting and bedding-plane slip on a growing anticline, and active tectonics of the Sistan suture zone. Geophys. J. Int. 142 (2), 283–299.

Blanpied, M.L., Lockner, D.A., Byerlee, J.D., 1995. Frictional slip of granite at hydrothermal conditions. J. Geophys. Res., Solid Earth 100 (B7), 13,045–13,064.

Chang, S., Wang, W., Lee, J., 2009. Modelling temporal variation of surface creep on the Chihshang fault in eastern Taiwan with velocity-strengthening friction. Geophys. J. Int. 176 (2), 601–613.

Copley, A., 2014. Postseismic afterslip 30 years after the 1978 Tabas-e-Golshan (Iran) earthquake: observations and implications for the geological evolution of thrust belts. Geophys. J. Int., ggu023.

den Hartog, S.A.M., Niemeijer, A.R., Spiers, C.J., 2012. New constraints on megathrust slip stability under subduction zone P–T conditions. Earth Planet. Sci. Lett. 353, 240–252.

Di Toro, G., Han, R., Hirose, T., De Paola, N., Nielsen, S., Mizoguchi, K., Ferri, F., Cocco, M., Shimamoto, T., 2011. Fault lubrication during earthquakes. Nature 471 (7339), 494–498.

Dieterich, J.H., 1979. Modeling of rock friction: 1. Experimental results and constitutive equations. J. Geophys. Res., Solid Earth 84 (B5), 2161–2168.

Ekström, G., Nettles, M., Dziewoński, A., 2012. The global CMT project 2004–2010: centroid-moment tensors for 13,017 earthquakes. Phys. Earth Planet. Inter. 200, 1–9.

Foroutan, M., Meyer, B., Sébrier, M., Nazari, H., Murray, A., Le Dortz, K., Shokri, M., Arnold, M., Aumaître, G., Bourlès, D., et al., 2014. Late Pleistocene–Holocene right slip rate and paleoseismology of the Nayband fault, western margin of the Lut block, Iran. J. Geophys. Res., Solid Earth 119 (4), 3517–3560. https://doi.org/10.1002/2013JB010746.

Goldsby, D.L., Tullis, T.E., 2002. Low frictional strength of quartz rocks at subseismic slip rates. Geophys. Res. Lett. 29 (17), 1844.

Goldsby, D.L., Tullis, T.E., 2011. Flash heating leads to low frictional strength of crustal rocks at earthquake slip rates. Science 334 (6053), 216–218.

Hillers, G., Ben-Zion, Y., Mai, P.M., 2006. Seismicity on a fault controlled by rate-and-state dependent friction with spatial variations of the critical slip distance. J. Geophys. Res., Solid Earth 111 (B1), B01,403.

Hirose, T., Shimamoto, T., 2005. Growth of molten zone as a mechanism of slip weakening of simulated faults in gabbro during frictional melting. J. Geophys. Res., Solid Earth 110 (B5), B05,202.

Ingleby, T., Wright, T., 2017. Omori-like decay of postseismic velocities following continental earthquakes. Geophys. Res. Lett. 44 (7), 3119–3130.

Jolivet, R., Lasserre, C., Doin, M.-P., Peltzer, G., Avouac, J.-P., Sun, J., Dailu, R., 2013. Spatio-temporal evolution of aseismic slip along the Haiyuan fault, China: implications for fault frictional properties. Earth Planet. Sci. Lett. 377, 23–33.

Kaneko, Y., Avouac, J.-P., Lapusta, N., 2010. Towards inferring earthquake patterns from geodetic observations of interseismic coupling. Nat. Geosci. 3 (5), 363–369.

Kato, N., 2004. Interaction of slip on asperities: numerical simulation of seismic cycles on a two-dimensional planar fault with nonuniform frictional property. J. Geophys. Res., Solid Earth 109 (B12), B12,306.

Kohlstedt, D., Evans, B., Mackwell, S., 1995. Strength of the lithosphere: constraints imposed by laboratory experiments. J. Geophys. Res., Solid Earth 100 (B9), 17,587–17,602.

Langbein, J., Murray, J.R., Snyder, H.A., 2006. Coseismic and initial postseismic deformation from the 2004 Parkfield, California, earthquake, observed by Global Positioning System, Electronic Distance Meter, Creepmeters, and Borehole Strainmeters. Bull. Seismol. Soc. Am. 96 (4B), 304–320.

Lin, J., Stein, R.S., 2004. Stress triggering in thrust and subduction earthquakes and stress interaction between the southern San Andreas and nearby thrust and strike-slip faults. J. Geophys. Res., Solid Earth 109 (B2).

Marone, C., 1998. Laboratory-derived friction laws and their application to seismic faulting. Annu. Rev. Earth Planet. Sci. 26 (1), 643–696.

Noda, H., Lapusta, N., 2013. Stable creeping fault segments can become destructive as a result of dynamic weakening. Nature 493 (7433), 518–521.

Okada, Y., 1985. Surface deformation due to shear and tensile faults in a half-space. Bull. Seismol. Soc. Am. 75 (4), 1135–1154.

Perfettini, H., Avouac, J.-P., 2004. Postseismic relaxation driven by brittle creep: a possible mechanism to reconcile geodetic measurements and the decay rate of aftershocks, application to the Chi-Chi earthquake, Taiwan. J. Geophys. Res., Solid Earth 109 (B2).

Philip, H., Meghraoui, M., 1983. Structural analysis and interpretation of the surface deformations of the El Asnam earthquake of October 10, 1980. Tectonics 2 (1), 17–49.

Rice, J.R., 2006. Heating and weakening of faults during earthquake slip. J. Geophys. Res., Solid Earth 111 (B5), B05,311.

Ruina, A., 1983. Slip instability and state variable friction laws. J. Geophys. Res., Solid Earth 88 (B12), 10,359–10,370.

Scholz, C.H., 1982. Scaling laws for large earthquakes: consequences for physical models. Bull. Seismol. Soc. Am. 72 (1), 1–14.

Segall, P., Bürgmann, R., Matthews, M., 2000. Time-dependent triggered afterslip following the 1989 Loma Prieta earthquake. J. Geophys. Res., Solid Earth 105 (B3), 5615–5634.

Şengör, A., Tüysüz, O., İmren, C., Sakınç, M., Eyidoğan, H., Görür, N., Le Pichon, X., Rangin, C., 2005. The North Anatolian fault: a new look. Annu. Rev. Earth Planet. Sci. 33, 37–112.

Shen, Z.-K., Sun, J., Zhang, P., Wan, Y., Wang, M., Bürgmann, R., Zeng, Y., Gan, W., Liao, H., Wang, Q., 2009. Slip maxima at fault junctions and rupturing of barriers during the 2008 Wenchuan earthquake. Nat. Geosci. 2 (10), 718.

Sibson, R.H., 1973. Interactions between temperature and pore-fluid pressure during earthquake faulting and a mechanism for partial or total stress relief. Nat. Phys. Sci. 243 (126), 66–68.

Spaans, K., Hatton, E., Gonzalez, P., Walters, R., McDougall, A., Wright, T., Hooper, A., 2017. Tectonic and volcanic monitoring using Sentinel-1: current status and future plans of the COMET InSAR portal. In: EGU General Assembly Conference Abstracts, vol. 19, p. 19397.

Thomas, M.Y., Avouac, J.-P., Champenois, J., Lee, J.-C., Kuo, L.-C., 2014a. Spatiotemporal evolution of seismic and aseismic slip on the Longitudinal Valley Fault, Taiwan. J. Geophys. Res., Solid Earth 119, 5114–5139.

Thomas, M.Y., Lapusta, N., Noda, H., Avouac, J.-P., 2014b. Quasi-dynamic versus fully-dynamic simulations of earthquakes and aseismic slip with and without enhanced coseismic weakening. J. Geophys. Res., Solid Earth 119, 1986–2004.

Thomas, M.Y., Bhat, H.S., Klinger, Y., 2017a. Effect of brittle off-fault damage on earthquake rupture dynamics. In: Thomas, M.Y., Mitchell, T.M., Bhat, H.S. (Eds.), Fault Zone Dynamic Processes: Evolution of Fault Properties During Seismic Rupture. John Wiley & Sons, Inc., pp. 255–280.

Thomas, M.Y., Avouac, J.-P., Lapusta, N., 2017b. Rate-and-state friction properties of the Longitudinal Valley Fault from kinematic and dynamic modeling of seismic and aseismic slip. J. Geophys. Res., Solid Earth 122 (4), 3115–3137.

Tsutsumi, A., Shimamoto, T., 1997. High-velocity frictional properties of gabbro. Geophys. Res. Lett. 24 (6), 699–702.

Verberne, B.A., Spiers, C.J., Niemeijer, A.R., De Bresser, J.H.P., De Winter, D.A.M., Plumper, O., 2014. Frictional properties and microstructure of calcite-rich fault gouges sheared at sub-seismic sliding velocities. Pure Appl. Geophys. 171 (10), 2617–2640.

Vernant, P., Nilforoushan, F., Hatzfeld, D., Abbassi, M., Vigny, C., Masson, F., Nankali, H., Martinod, J., Ashtiani, A., Bayer, R., et al., 2004. Present-day crustal deformation and plate kinematics in the Middle East constrained by GPS measurements in Iran and northern Oman. Geophys. J. Int. 157 (1), 381–398.

Walker, R., Jackson, J., Baker, C., 2003. Surface expression of thrust faulting in eastern Iran: source parameters and surface deformation of the 1978 Tabas and 1968 Ferdows earthquake sequences. Geophys. J. Int. 152 (3), 749–765.

Walker, R., Gans, P., Allen, M., Jackson, J., Khatib, M., Marsh, N., Zarrinkoub, M., 2009. Late Cenozoic volcanism and rates of active faulting in eastern Iran. Geophys. J. Int. 177 (2), 783–805.

Werner, C., Wegmüller, U., Strozzi, T., Wiesmann, A., 2000. GAMMA SAR and interferometric processing software. In: Proceedings of the ERS-Envisat Symposium, vol. 1620. Gothenburg, Sweden, p. 1620.

Wessel, P., Smith, W.H., 1998. New, improved version of Generic Mapping Tools released. Eos 79 (47), 579.

Wibberley, C.A., Yielding, G., Di Toro, G., 2008. Recent advances in the understanding of fault zone internal structure: a review. Geol. Soc. (Lond.) Spec. Publ. 299 (1), 5–33.

Zhou, Y., Walker, R.T., Hollingsworth, J., Talebian, M., Song, X., Parsons, B., 2016. Coseismic and postseismic displacements from the 1978 M_w 7.3 Tabas-e-Golshan earthquake in eastern Iran. Earth Planet. Sci. Lett. 452, 185–196.